ChemCatChem
Research Article
doi.org/10.1002/cctc.202300947
Chemistry Europe
European Chemical Societies Publishing

Systematic *in situ* Investigation of the Formation of NH_3 Cracking Catalysts from Precursor Perovskites ABO_3 (A = La,Ca,Sr and B = Fe,Co,Ni) and their Catalytic Performance

Simone Gallus[a] and Claudia Weidenthaler*[a]

This work addresses the formation of ammonia (NH_3) decomposition catalysts derived from perovskites ABO_3 (A = La, Ca, Sr, and B = Fe, Co, Ni) precursors via *operando* synchrotron X-ray diffraction experiments. During the reaction in NH_3, the perovskite precursors are decomposed and the transition metals are reduced. Depending on their reduction properties, active metallic catalysts are formed *in situ* on La_2O_3 as support. The reduction behavior of the perovskites, formation of intermediate phases during activation, and catalytic performance was studied in detail. In addition, microstructure properties such as crystallite sizes and particle morphology were analyzed. Co-/Ni-based perovskites decomposed completely during activation to Co^0/Ni^0 supported on La_2O_3 while Fe-based perovskites were fully stable but inactive in catalysis. This difference is due to varying electronic properties of the transition metals, e.g., decreasing electronegativity from Ni to Fe. With decreasing reducibility, the intermediate phases during activation formed more distinct. La^{3+} was partially substituted by Ca^{2+}/Sr^{2+} in $LaCoO_3$ to test for advantageous effects in NH_3 decomposition. The best performance was observed using the precatalyst $La_{0.8}Sr_{0.2}CoO_3$ with a conversion of 86% (100% NH_3, 15000 mL g^{-1} h^{-1}) at 550 °C.

Introduction

Creating energy storage possibilities and increasing their capacities are substantial challenges in today's society. This is an essential requirement to change from a fossil fuel-based energy industry to a sustainable and environmentally friendly one driven by renewable energy sources. A hydrogen-based energy economy could be an alternative to the current carbon-based one, where the energy is stored chemically in the form of hydrogen (H_2).[1] It has a higher weight-based energy density than fossil fuels and can be stored pure, in a liquid (1 bar, −253 °C) or pressurized (500 bar, 25 °C) state, or bound in compounds.[2] Examples for the latter are the hydrogen-carrier molecule ammonia (NH_3), metal-organic frameworks that can adsorb hydrogen on their surface, or metal hydrides that can take up hydrogen on the interstitial spaces of their crystal structures or form new phases. Compared to the other hydrogen storage options, ammonia has several advantages such as its high volumetric and gravimetric hydrogen storage densities.[3] These amount to 120 kgm^{-3} and, respectively, 17.65 wt-%.[4] Another advantage is the existing infrastructure and experience in transporting and storing ammonia.[5] As it is a base chemical for the production of fertilizers, it is a widely handled and essential product of today's chemical industry. In the case of using carrier substances, such as ammonia, catalytic processes are necessary for binding the hydrogen and rereleasing it for further utilization. The noble metal ruthenium was shown to be a very active catalyst for ammonia decomposition and has been studied extensively as a single catalytically active element, as well as in combination with transition metals.[6] However, it is highly desirable to find catalysts that consist only of less expensive and more abundant elements. Among the transition metals, nickel and cobalt have gained considerable interest and have been studied on various supports and prepared by different synthesis pathways.[7] One promising catalyst type is the decomposition product of perovskites ABO_3 gained after an activation procedure, as a first investigation has shown.[8] The idea for this method is based on a process called exsolution, during which the B-site cations, here transition metals, get reduced to their metallic state and diffuse towards the surface of the perovskite.[9] For the preparation of ammonia decomposition catalysts as in the above-mentioned studies, the reduction process is operated beyond the exsolution so that the perovskite completely decomposes and the transition metals B^0 remain on an oxide support A_xO_y. This strategy of catalyst preparation has several advantages compared to conventionally deposited nanoparticles on a support material. Problems like agglomeration, nonuniform spatial distribution, and poor control over the nanoparticle sizes can occur in catalysts synthesized by conventional methods, such as vapor deposition techniques or wet-chemical impregnation, resulting in fast catalytic deactivation.[9a] Catalysts prepared by exsolution have an exceptionally strong particle-support interaction,

---

[a] *S. Gallus, Prof. Dr. C. Weidenthaler*
Department of Heterogeneous Catalysis
Max-Planck-Institut für Kohlenforschung
Kaiser-Wilhelm-Platz 1, 45470 Mülheim an der Ruhr (Germany)
E-mail: weidenthaler@mpi-muelheim.mpg.de

Supporting information for this article is available on the WWW under https://doi.org/10.1002/cctc.202300947

hindering these processes.[10] This is due to their anchorage, meaning the nanoparticles are seated in an indentation on the support material.[11]

The aforementioned first study on employing perovskites as precatalysts for ammonia decomposition by Pinzon et al. (2021) used the compositions $LaNiO_3$ and $LaCoO_3$.[8] After synthesis via self-combustion, the perovskites were fully reduced with hydrogen to a metallic phase (Ni^0 or Co^0) on a lanthanum oxide (La_2O_3) support before catalytic testing. Small perovskite crystallites resulted in smaller well-dispersed Co^0/Ni^0 crystallites, enhancing the catalytic performance. Additionally, the $LaNiO_3$-derived catalyst displayed a higher conversion rate and had a lower determined apparent activation energy than the $LaCoO_3$-derived one, which was argued to be due to an improved nitrogen (N_2) desorption. This was explained by higher basicity measured for the initial perovskites. Besides the choice of the transition metal for the B-position in the perovskite ABO_3, the selection of the A element, which is part of the oxide support for the metallic catalytic phase after activation, is of great importance regarding catalyst-support interactions that can influence catalytic performances significantly.[12] The partial substitution of lanthanum with cerium and magnesium in cobalt- and nickel-based perovskites ($La_yA_{1-y}Co_xNi_{1-x}O_3$, A = Ce, Mg) serving as precatalysts for ammonia decomposition has been examined.[13] The accordingly derived catalysts were shown to result in higher catalytic activity upon partial substitution of lanthanum. The reasons were an enhanced decrease in crystallite size of the metallic phase, improving its dispersion, and further facilitating the nitrogen desorption, which is the conversion rate-limiting step during ammonia decomposition for non-noble-metals.[13b,14] Additionally, cerium was reported to enhance the reducibility of the transition metals.[13a] A different system, in which perovskite-supported cobalt catalysts were tested for ammonia cracking, has been examined using several other elements (Mg, Ca, Sr, Ba) occupying the A-site in $XCeO_3$.[15] This study also found that doping enhanced the reducibility of the transition metals with increasing extent going from magnesium to barium. The addition of the strong alkaline earth metal reportedly promoted electron conductivity and adapted the binding energy of the active site and the nitrogen atoms for optimized catalytic performance. Another study, which employed the perovskite $LaAlO_3$ as the support material for a ruthenium catalyst, found that substituting one-fifth of lanthanum with strontium led to an electron-rich state of the ruthenium. This facilitated nitrogen desorption and accelerated ammonia decomposition.[12c] The results of these past reports strongly encourage testing even more elements for lanthanum substitution on the A-site in the perovskite for their potential to modify the electronic state of the catalysts advantageously.

In this work, we investigate the activation process of cobalt/nickel-based lanthanum-containing perovskite precatalysts and follow the *in situ* formation of the final catalysts for ammonia decomposition via intermediate phases for a detailed analysis of the structure-property relationships. In the previous studies by Pinzon et al. and Podila et al. on La-based perovskites as precatalysts for ammonia decomposition, the perovskites and the catalysts were analyzed after activation, but not how exactly the activation proceeds, which is the focus of this work.[8,13] In addition, Pinzon and co-workers used only very low NH_3 concentrations of 5% in the reactant gas, whereas we use 100% NH_3 in our work. Another difference from previous studies is the activation of the catalysts. In all studies, the perovskite precursors were first reduced in hydrogen at high temperatures (550–600 °C) for several hours. In our experiments, we will observe the temperature-dependent conversion of the perovskite precursor and the formation of the active metal species *in situ* under reaction conditions in NH_3. As an outlook for future studies optimizing the catalytic performance, the effect of substituting one-fifth of lanthanum, once with calcium and once with strontium, in the sample $LaCoO_3$ is additionally analyzed. The perovskites were synthesized by incipient wetness impregnation of microporous carbon spheres with metal nitrate solutions and subsequent calcination. The successful synthesis was confirmed by powder X-ray diffraction. Temperature-programmed reduction (TPR) experiments were conducted to analyze the reduction behavior of the perovskites. Catalytic tests consisted of plug-flow reactor experiments to evaluate the conversion rate accurately and were followed by collecting electron microscopy images of the samples after the reaction. *Operando* synchrotron powder diffraction experiments under catalytic reaction conditions (100% NH_3) provided the necessary time resolution to track the formation of the catalyst in detail.

Results and Discussion

Characterization of the Perovskite Precursors

Perovskites of various lanthanum-based compositions have been successfully synthesized via the incipient wetness impregnation method. The results of the in-house X-ray powder diffraction experiments are shown in Figure 1. As expected, the perovskites ABO_3 adopt different crystal symmetries depending on their composition. This distortion of the pristine cubic

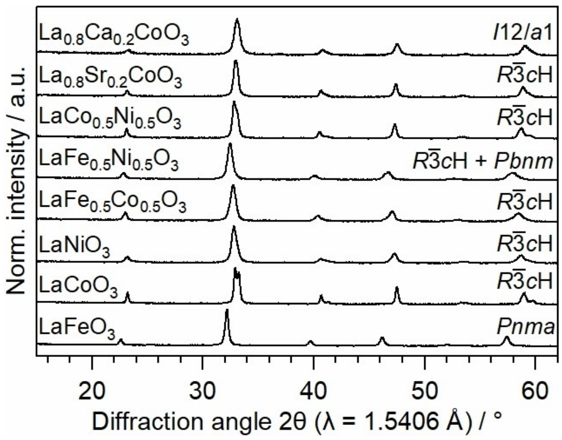

Figure 1. In-house measured X-ray diffractograms of all synthesized perovskites, given with their respective chemical composition and space group.

perovskite structure is due to the varying sizes of the ions occupying the sites in the crystal structure.[16] Therefore, perovskites of the compositions $LaB_{0.5}B'_{0.5}O_3$ with B = B′ = Fe, Co, Ni, and $La_{0.8}A_{0.2}CoO_3$ with A = Ca, Sr display crystal symmetries ranging from monoclinic, via orthorhombic, to rhombohedral. Besides the identified main perovskite phase, impurities of 2-3 wt-% transition metal oxides can be present. Depending on the sample composition, these are Fe_xO_y, NiO, or Co_3O_4. Detailed Rietveld refinement results are given in the supporting information in Table S1.

Hydrogen-TPR experiments were performed on all synthesized perovskites to determine their reducibility. Due to their large ionic radius and low electronegativity, La^{3+} ions are not reducible under the given experimental conditions. Moreover, La_2O_3, one of the final phases after TPR, is a strongly basic oxide. Therefore, all hydrogen consumption can be assigned to the reduction of transition metal species.

For the compositions $LaNiO_3$ and $LaCoO_3$, a similar shape of the thermal conductivity detector (TCD) signal curve with two major reduction events can be observed (Figure 2a), which is in agreement with literature reports.[17] $LaNiO_3$ shows easier reducibility than $LaCoO_3$, as its reduction was finished at approximately 550 °C, while $LaCoO_3$ was fully reduced at around 600 °C. Compared to cobalt, this is due to the higher electronegativity of nickel, resulting in a higher degree of hybridization of the transition metal 3*d*-O 2*p* states and, thus, increased covalency.[18] Previous studies show that $LaCoO_3$ is predominantly a small-band-gap charge-transfer insulator, while $LaNiO_3$ has a metallic electronic character.[19] For both compositions, the first major reduction event represents the reduction of the transition metal ion on the B-site (B = Co, Ni) from B^{3+} to B^{2+}, which correlates to a phase change from $LaBO_3$ to $La_2B_2O_5$. $La_2B_2O_5$ is a brownmillerite-type phase that has been observed as a nickel- and cobalt-based structure and can be described as an oxygen-deficient perovskite.[17c,20] However, this first signal displays a small shoulder for both perovskites in our study. Observations of such a TCD profile shape have been reported in part of previous publications, though various reasons are given for this reduction behavior. One possible explanation is the formation of an additional phase, $La_3B_3O_8$, an intermediate between brownmillerites and perovskites.[20] Another interpretation for the reaction could be the reduction of the impurity phase NiO ($Ni^{2+} \rightarrow Ni^0$), as its reduction starts at a temperature similar to that of $LaNiO_3$.[21] Equivalently, the small shoulder in the measurement of the cobalt-based perovskite could be due to the reduction of the Co_3O_4 impurity to CoO ($Co^{3+} \rightarrow Co^{2+}$).[22] Furthermore, a comparison of nanocast and conventionally synthesized perovskites via citric acid gave Nair et al. (2014) reason to assume that further reduction of nickel in grain boundaries led to the formation of the shoulder, as it was not present for the nanocast material.[17c] A fourth explanation might be the early formation of B^0 in parallel to the B^{3+} to B^{2+} reduction step, as reported by Ivanova et al. (2010).[17b] Their study found a decrease in the ideal ratio 1 : 2 of the areas below the first ($B^{3+} \rightarrow B^{2+}$) and the second reduction event at higher temperatures. This second event is consistently reported to correspond with the final reduction step from B^{2+} to B^0 in the literature. After complete reduction, the final phase composition is La_2O_3 and B^0.[17c,23] Echchahed et al. (2006) also reported the early formation of B^0 and correlated it to the volume of hydrogen consumed between the two major reduction peaks.[17a] This increase of the minimum between both peaks can be seen especially for $LaNiO_3$ in Figure 2a, which also displays the more pronounced shoulder compared to $LaCoO_3$.

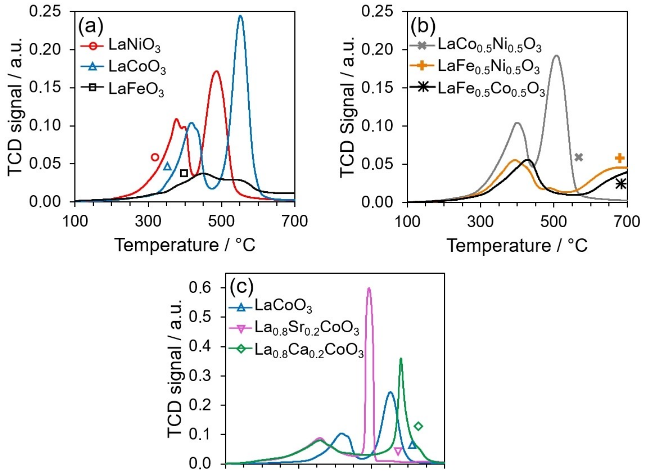

Figure 2. TPR curves for the precatalysts of different perovskite compositions (a) ABO_3; (b) B-site substituted; and (c) A-site substituted.

In contrast, $LaFeO_3$ displays a very different reduction behavior with two much smaller and broader peaks in the 350–650 °C range and an unfinished reduction process at 700 °C. It can be easily estimated that compared to $La(Co,Ni)O_3$, a significantly lower amount of hydrogen was consumed, which indicates that the $LaFeO_3$ crystal structure was stable in the reductive atmosphere in this temperature range. Spinicci et al. (2002) have reported a similar, very shallow TCD profile in the same temperature range.[24] Provendier et al. (1999) found $LaFeO_3$ nearly irreducible.[25] This behavior can be explained by $LaFeO_3$'s electronic structure and iron having the lowest electronegativity compared to cobalt and nickel. According to Arima et al. (1993), $LaFeO_3$ is considered to be an intermediate charge-transfer/Mott-Hubbard insulator.[26] A possible explanation for the observed hydrogen consumption is given by Ciambelli et al. (2001). They identified a low amount of Fe^{4+} to Fe^{3+} reduction while measuring their $LaFeO_3$ sample and explained the small presence of Fe^{4+} ions by charge transfer and associated oxygen deficiency in the perovskite structure.[27] Besides, our study's sample contains a Fe_2O_3 impurity of approximately 2 wt-%, which is known to reduce via Fe_3O_4 and FeO to Fe^0 in the temperature range in question and added to the TCD signal.[28]

The mixed iron-cobalt-nickel-containing perovskites (Figure 2b) show a combination of the characteristics observed so far, exhibiting the stabilizing influence of iron in the perovskite structure. Both samples, $LaFe_{0.5}Ni_{0.5}O_3$ and $LaFe_{0.5}Co_{0.5}O_3$, display better reducibility than $LaFeO_3$ but worse than $LaNiO_3$ and $LaCoO_3$. Similarly, two major reduction events can be seen for the iron-cobalt- and iron-nickel-based perovskites. However, the second one is shifted to a much higher temperature of approximately 600 °C and continues outside the measured range. Both TPR peaks are significantly smaller, which leads to the assumption that only Co^{3+}/Ni^{3+} was reduced to Co^{2+}/Ni^{2+} during the first reduction event, while Fe^{3+} was stable. This is in agreement with the literature.[17b,29] For TPR experiments of similar iron-nickel-based perovskites, Provendier et al. (1999) have assigned the second peak to the reduction of nickel and part of the iron to the metallic state, forming a nickel-iron alloy.[25] It is reasonable to assume an analogous process for $LaFe_{0.5}Co_{0.5}O_3$, with the starting formation of a cobalt-iron alloy in the high-temperature range of our experiment. The TPR profile of $LaCo_{0.5}Ni_{0.5}O_3$ appears like an averaged curve between the pure nickel- and cobalt-based perovskites concerning the temperatures of the peak positions. The same reduction steps as for $LaCoO_3$ and $LaNiO_3$ can be correlated to the peaks, with the first representing the formation of a brownmillerite phase containing both cobalt and nickel ($B^{3+} \rightarrow B^{2+}$). The reduction to metallic cobalt and nickel is attributed to the second peak. As Ivanova et al. (2010) have explained, whether pure Co^0 and Ni^0 phases are present or an alloy of both cannot be determined without advanced methods.[17b] A simple ex-situ X-ray diffraction measurement would be insufficient due to the broadness of the metal Bragg reflections and their very close positions due to similar lattice parameters. The partial substitution of lanthanum by strontium or calcium (Figure 2c) in the cobalt-based perovskite changes the reduction behavior immensely. Nevertheless, the presence of two major reduction events is still given. For $La_{0.8}Ca_{0.2}CoO_3$ and $La_{0.8}Sr_{0.2}CoO_3$, the first one is broadened and shifted from its peak at 400–450 °C for $LaCoO_3$ to 350 °C. Again, this peak correlates with the reaction from Co^{3+} to Co^{2+}. However, substitutions with strontium and calcium have a very different influence on the second reduction event. In the case of calcium substitution, this reduction peak is sharpened and shifted from 550 °C ($LaCoO_3$) to a higher temperature of 580 °C. It is asymmetric with a continued hydrogen consumption up to 650 °C. In contrast, the second TPR reduction peak for the strontium-containing sample is moved to a lower temperature of 500 °C. Moreover, it is very sharp, indicating an abrupt reduction. As for $LaCoO_3$, these second reduction events represent the formation of Co^0. In the case of calcium and strontium substitution, a trivalent (La^{3+}) ion is replaced with a divalent ion (Ca^{2+}, Sr^{2+}). Hence, compensation processes must take place to preserve charge neutrality. These can be the formation of tetravalent cobalt ions and oxygen deficiencies.[30] The advantages are increased oxygen mobility, enhanced redox properties, and, thus, easier reducibility.[30b,31] This can explain the shift of the first reduction step to lower temperatures compared to $LaCoO_3$. Rojas et al. (2022) have further determined that forming Co^{4+} ions is the preferred charge compensation process when lanthanum is substituted with strontium.[32] Contrarily, oxygen vacancies are preferred for substitution with calcium.[32] This difference might be why the final reduction step to metallic cobalt happens at lower temperatures when the sample contains strontium than calcium. Additionally, it was reported that incorporating strontium in the perovskite structure leads to a smaller crystallite size and a less crystalline perovskite, further adding to easier reducibility.[33]

In situ NH_3 Decomposition XRD

After an initial characterization of the different perovskite compositions, several were chosen to be investigated with *in situ* methods and detailed catalytic testing. The basic ones, $LaFeO_3$, $LaCoO_3$, and $LaNiO_3$, were selected to gain a fundamental understanding of their behavior with each transition metal occupying the B-site. The perovskites $La_{0.8}Ca_{0.2}CoO_3$ and $La_{0.8}Sr_{0.2}CoO_3$ raised interest due to their easy reducibility in the TPR measurements, which is why they were also examined to gain an initial understanding of how substitutions on the A-site might influence the reaction behavior and the catalytic performance.

These five perovskites were investigated with *operando* synchrotron X-ray powder diffraction experiments under catalytic reaction conditions (100% NH_3, 25–650 °C) with simultaneous gas analysis. Thereby, a qualitative determination of the conversion for ammonia cracking is possible. The diffraction data analysis was performed via Rietveld refinements. This enables monitoring the phase development during the first heating cycle of the experiment when the perovskite precatalyst is activated, and the active catalyst phase is formed. However, due to the highly dynamic character of the samples with simultaneous formation and decomposition of intermediate phases during the experiment, the analysis via Rietveld refinements is very difficult. Even though data collection time per frame was 60 sec, the processes are very fast and one can only get a qualitative snapshot. Thus, the derived weight percentages should preferably be taken for a qualitative evaluation and pointing out tendencies rather than giving exact quantitative phase compositions. For $LaCoO_3$ (space group $R\bar{3}cH$, No. 167), the plot of raw data for both the activation and catalytic cycle and selected significant diffractograms collected at various temperatures during activation are shown in Figure 3.

The first phase that formed after the perovskite in the reducing ammonia atmosphere was an oxygen-depleted perovskite with the structural formula $La_3Co_3O_8$ (space group $P12_11$, No. 4) at approximately 400 °C. This phase was first described by Grenier et al. (1976). It is characterized by ordered oxygen vacancies that result in cobalt being coordinated not exclusively octahedrally but also tetrahedrally.[34] In parallel, the small impurity phase Co_3O_4 (space group $Fd\bar{3}mZ$, No. 227) was reduced via CoO (space group $Fm\bar{3}m$, No. 225) to metallic cobalt (space group $Fm\bar{3}m$, No. 225) started forming at approximately 450 °C. $La_3Co_3O_8$ was further reduced to the brownmillerite phase $La_2Co_2O_5$ (space group *Pnma*, No. 62). This intermediate phase also had a measurable contribution to the TPR curve and was discussed in its analysis. This might be due to its thermal stability over a broader temperature range than $La_3Co_3O_8$, as the continuous phase development indicates (SI Figure S1). Concerning the crystal structure, $La_2Co_2O_5$ contains only Co^{2+} ions and no more Co^{3+} ions,[35] as visible in the schematic phase development during activation in Scheme 1.

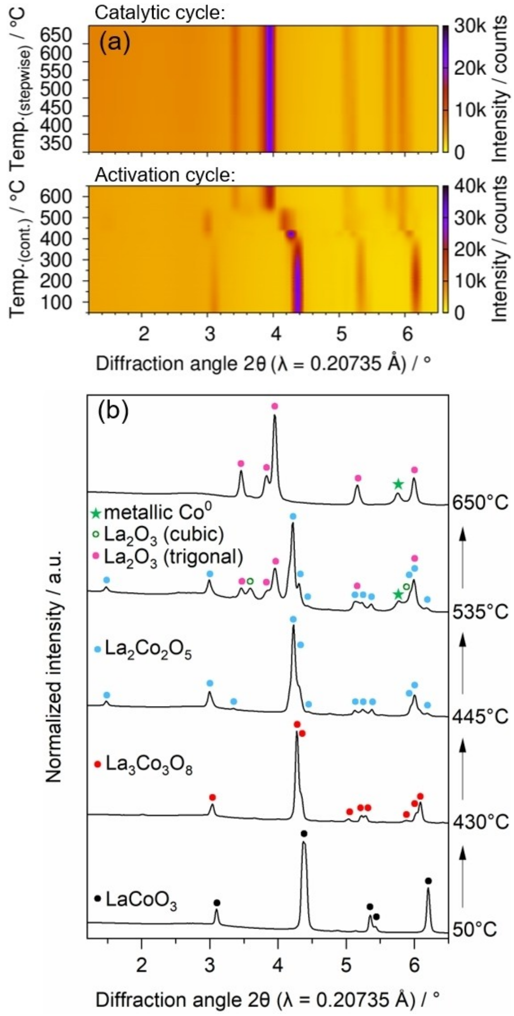

Figure 3. (a) *In situ* synchrotron data collected during the activation and the first catalytic cycle of NH_3 decomposition using the precatalyst $LaCoO_3$; (b) most important diffractograms observed at selected temperatures during the activation and the respectively identified phases.

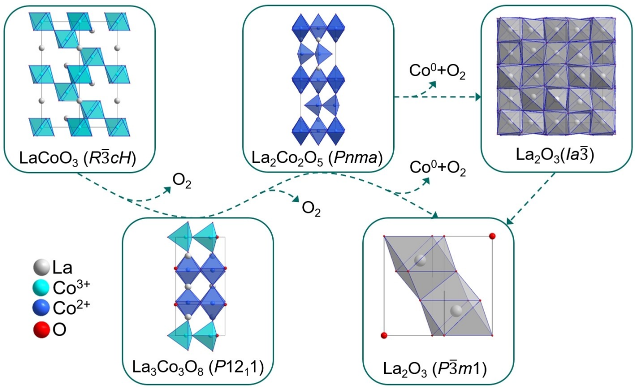

Scheme 1. Schematic phase development during the activation cycle of the precatalyst $LaCoO_3$ in NH_3 atmosphere.

The decomposition of this phase leads to the final reduction products Co^0 and La_2O_3. Lanthanum oxide usually adopts a trigonal crystal structure (space group $P\bar{3}m1$, No. 164), which was observed to be present at the end of the activation process of all examined perovskite compositions. However, when using $LaCoO_3$ as a precursor, the additional crystallization of a metastable cubic lanthanum oxide can be observed simultaneously with the trigonal one upon heating during the *operando* experiments. Few publications mentioning cubic lanthanum oxide discuss possible space groups, which also do not necessarily agree with each other, so the structure has not been determined without a doubt yet.[36] Nevertheless, there seems to be a consensus for a body-centered space group.[36b,c,37] For the analysis in this study, a crystal structure published by Felsche et al. (1969) with the space group $Ia\bar{3}$ (No. 206) is assumed.[37] Glushkova et al. (1963) were the first to describe the formation of cubic lanthanum oxide.[38] Others later examined the formation, for example, from lanthanum nitrate upon heating with a specific rate at approximately 550 °C. However, they found it to quickly transform into a trigonal crystal structure at higher temperatures due to high instability.[39] In agreement with the literature, this cubic La_2O_3 phase disappeared again in our experiment upon further heating at approximately 600–700 °C, and the trigonal crystal structure formed instead.[40] The appearance of this metastable lanthanum oxide phase in the case of precatalysts $LaCoO_3$ indicates a slower reduction process compared to activation of the other perovskite compositions, where this phase did not appear.

In comparison, the phase development during the activation of $La_{0.8}Sr_{0.2}CoO_3$ shows significant differences. This is evident from the plot of raw data for both the activation and catalytic cycle and selected significant diffractograms collected at various temperatures during activation shown in Figure 4. The first decomposition step appeared approximately 100 °C earlier at 300 °C compared to 400 °C observed for $LaCoO_3$ (SI Figure S2). Additionally, the oxygen-depleted perovskite could not be identified in the diffraction pattern. Instead, the formation of a brownmillerite-type phase could be observed as the first identifiable intermediate decomposition product. No crystal structure is published for such a phase containing strontium; therefore, the published $La_2Co_2O_5$ structure is manually adapted by modifying the occupancies in the Rietveld refinements to exchange one fifth of cobalt by strontium. The difference in oxidation state between La^{3+} and Sr^{2+} ions likely leads to an increase in the average oxidation number for cobalt ($Co^{2.2+}$ in $La_{1.6}Sr_{0.4}Co_2O_5$ vs. Co^{2+} in $La_2Co_2O_5$). The reason for this assumption is the knowledge that the oxidation state of cobalt adjusts to very common nonstoichiometric oxygen occupancies in the perovskite structure leading to the distinct $La_2Co_2O_5$ and $La_3Co_3O_8$ phases. The missing crystallization of a phase similar to $La_3Co_3O_8$ with strontium substitution and the abrupt complete reduction of the brownmillerite phase shortly below 500 °C emphasize the strong reducibility gained by introducing strontium in the system. This tendency was also observed with the reduction behavior in the TPR measurements and agrees with literature reports.[41] Accordingly, substituting lanthanum with strontium in iron-nickel-based perovskite precatalysts was reported to result in increased reducibility and segregation of nickel to the surface during exsolution.[42] The

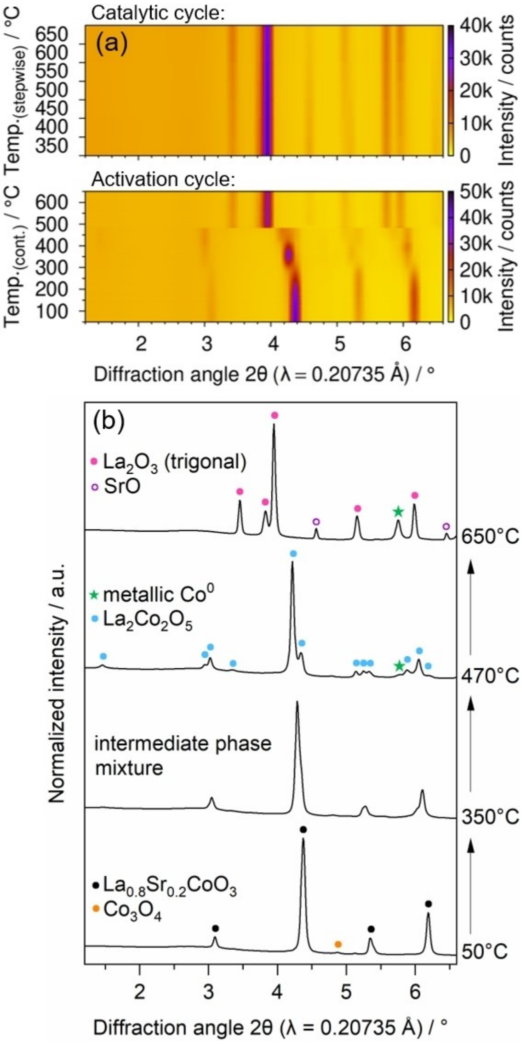

Figure 4. (a) *In situ* synchrotron data collected during the activation and the first catalytic cycle of NH_3 decomposition using the precatalyst $La_{0.8}Sr_{0.2}CoO_3$; (b) most important diffractograms observed at selected temperatures during the activation and the respectively identified phases.

final reduction products were La_2O_3, SrO, and Co^0, as shown by the schematic phase development during activation (Scheme 2).

The raw data and derived phase developments during the activation cycle of the other perovskite compositions are shown in the supporting information (SI Figure S3 to Figure S5). It is worth mentioning that for $La_{0.8}Ca_{0.2}CoO_{3,}$ the oxygen-depleted perovskite and the brownmillerite phase could be observed. Due to a lack of published crystal structure data with calcium substitution, both are manually adapted versions of the pure lanthanum-cobalt-based versions described in the literature. The formation of both phases shows the slightly lower reducibility and slower reduction speed of this perovskite composition compared to the strontium-substituted perovskite. As expected, $LaFeO_3$ did not decompose, while the Fe_2O_3 impurity was reduced and reacted to iron nitrides in the ammonia atmosphere. These nitrides are active catalysts for ammonia cracking.[43] $LaNiO_3$ was found to contain stacking faults of the Ruddlesden-Popper-type (LaO-LaO shear faults), which made the accurate phase analysis difficult because of shifted and asymmetric Bragg reflections. (A publication describing a $LaNiO_3$ model containing these stacking faults that can be used for refining diffraction data is currently in preparation.) A phase mixture of two brownmillerite phases (of which one is a published cobalt-containing phase that is manually substituted with nickel), three different published Ruddlesden-Popper phases, and NiO was approximated to appear between the initial perovskite and the final reduction products, La_2O_3 and Ni^0. The publication references of the used crystal structures can be found in the experimental description. The simultaneous existence and transformation of these phases prove how dynamic the system is and again display that nickel can be reduced easily.

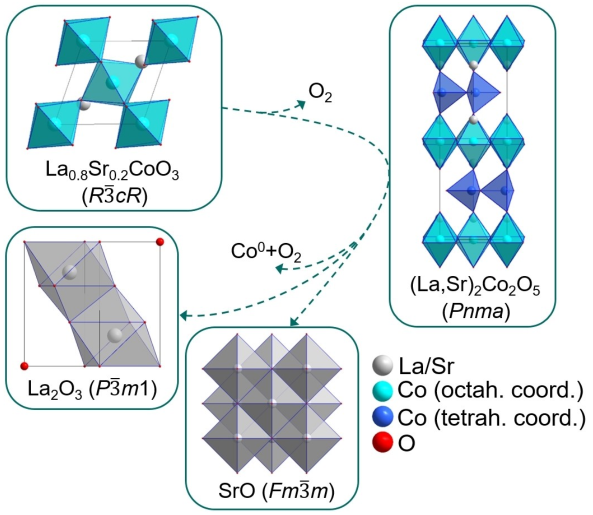

Scheme 2. Schematic phase development during the activation cycle of the precatalysts $La_{0.8}Sr_{0.2}CoO_3$ in NH_3 atmosphere.

After the activation cycle, the phase composition does not change during the catalytic cycles in all experiments. As metallic cobalt or nickel formed during the activation, an increasing conversion for ammonia cracking was measured. This is direct evidence that the metallic state of the transition metal catalysts is decisive for the catalytic activity. The conversion curves obtained during the catalytic ammonia decomposition cycles are shown in Figure 5. Based on these experiments, a detailed quantitative discussion is impossible, as an undefined sample volume was heated in the capillary by the hot air blower, and a fixed gas flow of 5 $mLmin^{-1}$ 100% NH_3 was applied. Nevertheless, certain tendencies can be observed that are later confirmed by a dedicated catalytic characterization in the section "Catalytic Testing". The precatalyst $LaFeO_3$ resulted in the lowest conversion, while the catalyst derived from the $La_{0.8}Sr_{0.2}CoO_3$ perovskite displayed the highest conversion. An improved catalytic performance upon strontium substitution has also been observed for other reactions due to increased reducibility and number of active species.[30b] Incorporating the transition metal nickel in the perovskite precursor resulted in

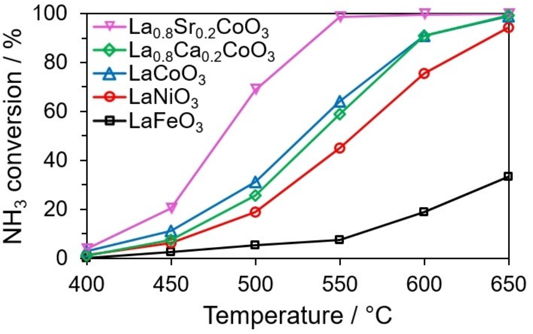

Figure 5. Qualitative proof of NH_3 conversion measured during *operando* synchrotron experiments using various perovskites as catalyst precursors with a fixed gas flow of 5 mLmin^{-1} 100 % NH_3 and approximately the same sample amounts of each perovskite; the calculation is based on the gas analysis by mass spectrometry measurements.

lower conversion rates for ammonia decomposition than when cobalt-based perovskites were tested.

Besides the phase composition, crystallite sizes have been determined. Instead of the limited usefulness of the Scherrer algorithm, the diffraction data were analyzed using whole powder pattern modeling (WPPM). So-called column length distributions are obtained for the crystalline materials from structure-independent line profile analysis.[44] This means that a lognormal distribution of column lengths is presumed for the crystalline domains of each phase. Such a column length distribution analysis provides a more detailed description of the actual state of crystallites in the sample. It is closer to reality than a traditional crystallite size analysis via the Scherrer method. The Scherrer equation gives an averaged volume-weighted value for the size based on the Bragg peak width, described by the integral breadth (IB) at any diffraction angle 2θ in the diffraction pattern. Using several Bragg peaks followed by a final averaging step instead of performing the calculation based on just one peak is advantageous; nevertheless, the Scherrer method disregards any influence of crystallite size distributions, strain, or anisotropic peak broadening on the peak shape.

Here, WPPM is performed on data collected at 650 °C at the end of the second catalytic cycle. The catalytic results and descriptions of the experiment come later in the text but at this point it should be mentioned that the samples went through an activation cycle and one catalytic cycle. From the end of the activation to the end of the catalytic cycle a small increase in crystallite size of a few nanometers for the present phases can be observed, which is shown exemplary for $LaNiO_3$ as the starting material (SI Figure S6). As $LaFeO_3$ did not decompose, it is excluded. For the other samples, the main phases at this point of the experiment were La_2O_3 and Co^0/Ni^0. The results of this analysis are shown in Figure 6. It can be seen that the column length distribution curves for the transition metal phases are relatively similar, with a median of approximately 10(2) nm. The exception is cobalt derived from $LaCoO_3$, which has a slightly narrower distribution and a median value shifted to 6–7 nm.

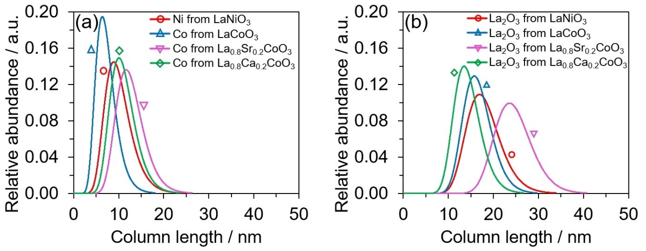

Figure 6. Column length distribution for the crystallites of the phases (a) Co/Ni and (b) La_2O_3 obtained during the catalytic cycle at 650 °C from the *operando* synchrotron data at DESY; the legend shows from which precursor the phases have formed.

Additionally, we have analyzed the crystallite size of the lanthanum oxide support. There is a distinct difference for this phase derived from the strontium-substituted perovskite compared to the other compositions, as its column length distribution is shifted to significantly higher values. This indicates that the precatalyst $La_{0.8}Sr_{0.2}CoO_3$ results in the highest difference in crystallite size between the active metal phase and its support. This might play an essential role in the superior catalytic performance of the strontium-containing sample due to the high significance of support-catalyst interactions in catalysis. Possible reasons for the differences in column length distributions among all samples could be the varying reaction speed and reaction pathways observed with diffraction during the *operando* experiments.

Catalytic Testing

The results of the catalytic testing of all perovskite precatalysts for ammonia decomposition in a plug-flow reactor are shown in Figure 7. The temperature 550 °C was chosen to compare the conversion of all samples at a given temperature. For simplification, the original perovskite formulas are further used as sample identifier even though most of the perovskites are decomposed and the activated catalysts are always reduced metals on La_2O_3 supports.

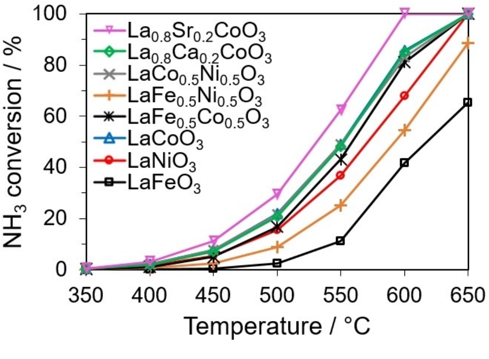

Figure 7. Conversion curves from the 3rd heating cycle of all perovskite compositions measured in a plug-flow reactor with a 100 % NH_3 gas flow (weight hourly space velocity of 15000 mL g^{-1} h^{-1} calculated based on the amount of weighed-in perovskite powder).

In agreement with the previously discussed TPR data, $LaFeO_3$ displays the lowest conversion of 11 % at 550 °C. Besides the iron oxide impurity, the precursor did not reduce under the selected reaction conditions, so the iron stayed trapped in the perovskite structure and could not reduce to form the active metal catalyst. Consistent with the previous TPR experiments, the substitution of cobalt/nickel with iron results in a decreased conversion ($LaNiO_3$: 37 %, $LaFe_{0.5}Ni_{0.5}O_3$: 25 %, $LaCoO_3$: 49 %, $LaFe_{0.5}Co_{0.5}O_3$: 43 %), as iron prevents the activation of the perovskite precatalyst. $LaCoO_3$, $LaCo_{0.5}Ni_{0.5}O_3$, and $La_{0.8}Ca_{0.2}CoO_3$ have the same conversion of around 49 % at 550 °C. The precatalyst $La_{0.8}Sr_{0.2}CoO_3$ results in the highest conversion of 62 % at 550 °C.

From the *operando* diffraction experiments with simultaneous gas analysis performed at the synchrotron, it is evident that only the metallic transition metals, which formed during the reduction of the perovskite, were the active phases for ammonia decomposition. Therefore, conversion measurements in the reactor were repeated for all sample compositions that were able to fully reduce during the activation; however, now the weight hourly space velocity is calculated based on the amount of the transition metal (Co/Ni) in the perovskite structure and not the whole perovskite. The conversion curves of these measurements are shown in the supporting information (SI Figure S7).

Via Arrhenius-type equation fitting, the apparent activation energy E_a [$kJmol^{-1}$] and the pre-exponential factor A [s^{-1}] were derived (Table 1). The corresponding Arrhenius plots can be found in the supporting information (SI Figure S8). The lowest apparent activation energy of 90 $kJmol^{-1}$ was determined for the catalyst derived from $LaNiO_3$. Nevertheless, this catalyst does not result in the highest conversion compared to the others due to having the lowest pre-exponential factor A of 4160 s^{-1}. In comparison, the catalyst derived from $LaCoO_3$ leads to a slightly higher apparent activation energy of 95 $kJmol^{-1}$ and also a higher pre-exponential factor A of 7801 s^{-1}. This is in agreement with smaller crystallite sizes for cobalt compared to nickel resulting in larger surface areas and therewith a higher number of active centers. Substituting half of the cobalt with nickel does not lower the resulting apparent activation energy compared to the catalyst derived from pure cobalt-based perovskite. Still, this mixed B-position in the precatalysts seems to slightly increase the pre-exponential A factor to 8183 s^{-1}.

The test of partially substituting lanthanum with calcium revealed interesting changes in the catalytic activity. Partial substitution with calcium does not influence the final apparent activation energy. Still, it lowers the pre-exponential factor A to 6003 s^{-1}, resulting in the worst-performing catalyst of the five examined samples. When using the precatalyst $La_{0.8}Sr_{0.2}CoO_3$, the observations made for the nickel-based catalyst are reversed. This strontium-substituted perovskite yields the catalyst with the highest required apparent activation energy of 100 $kJmol^{-1}$ but also the highest factor A, which is 2.5 to 5 times higher than for the other samples with 20684 s^{-1}. Thus, the value of the pre-exponential factor A compensates for the highest E_a among all samples, making it the catalyst with the highest conversion for ammonia decomposition.

Table 1. Catalyst precursors with the corresponding calculated apparent activation energies E_a and the pre-exponential factors A derived from the Arrhenius plots.

Catalyst precursor	E_a/$kJmol^{-1}$	A/s^{-1}
$LaNiO_3$	90	4160
$La_{0.8}Ca_{0.2}CoO_3$	94	6003
$LaCo_{0.5}Ni_{0.5}O_3$	95	8183
$LaCoO_3$	95	7801
$La_{0.8}Sr_{0.2}CoO_3$	100	20684

Testing these five samples after three heating cycles in the plug-flow reactor for their stability during ammonia decomposition for 20 h at 550 °C shows that only the catalyst derived from $LaCoO_3$ is entirely stable. The $La_{0.8}Ca_{0.2}CoO_3$- and $LaNiO_3$-based catalysts have a conversion loss of 1 %, while the $LaCo_{0.5}Ni_{0.5}O_3$- and $La_{0.8}Sr_{0.2}CoO_3$-based catalysts display a loss of 2 % (Figure 8). The reason could be slight crystallite growth effects over a prolonged time at elevated temperatures. This has been observed on a small scale during the *operando* catalytic experiments (SI Figure S6).

Our catalytic testing results agree with the tendencies reported in the literature. Previous studies on using perovskites as precatalysts for ammonia decomposition confirm our observation that $LaNiO_3$ results in a catalyst having a lower needed apparent activation energy E_a than $LaCoO_3$.[8,13b] Unfortunately, the catalytic behavior cannot directly be related to our studies, because only 5 v/v% NH_3 have been used while in the present study the feed gas contained 100 % NH_3.

Different promoters have been tested for their influence on ammonia decomposition ranging from the earth alkali metals magnesium, calcium, strontium, and barium to the rare earth metal cerium. It was shown that the partial substitution of lanthanum with magnesium leads to a more substantial increase of the catalytic activity in $LaNiO_3$ than with cerium, though both elements have an increasing effect on the conversion.[13] A positive influence on ammonia decomposition by strontium substitution in a $LaAlO_3$ perovskite acting as the support for ruthenium particles has been observed and ascribed

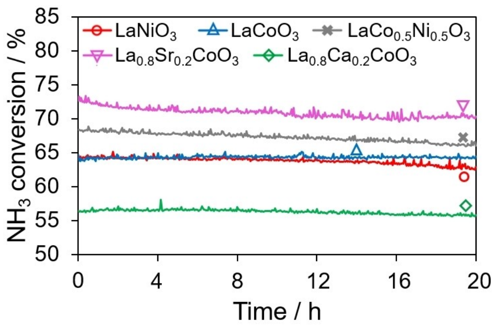

Figure 8. Conversion stability test for 20 h at 550 °C for NH_3 cracking after three heating cycles in a plug-flow reactor with various perovskites used as the catalyst precursor; measured with a 100 % NH_3 gas flow, a weight hourly space velocity of 15000 $mL\,g^{-1}\,h^{-1}$ calculated based on the amount of Co/Ni contained in the used perovskite sample.

to the modulation of the electronic properties by a strong metal-support interaction and a resulting electron-rich state of the ruthenium particles.[12c] The systematic study of different alkaline earth metals in $XCeO_3$ perovskites ($X = Mg$, Ca, Sr, Ba) serving as the support for cobalt catalysts exhibited the correlation of the catalytic activity with the decrease in electronegativity of the alkaline earth metals with the barium-containing sample displaying the highest conversion.[15] Simultaneously, the reducibility of cobalt was shown to increase with the period of the earth alkali element incorporated in the support. The explanation given was the promotion of the electron conductivity leading to an adjusted binding energy of the active site to the nitrogen atom from the ammonia molecule. Such positive effects can be presumed to be present for the best-performing catalyst in our study, which is the cobalt-catalyst supported on La_2O_3 and SrO derived from the $La_{0.8}Sr_{0.2}CoO_3$ perovskite.

After the conversion and stability measurements in the plug-flow reactor, these samples were analyzed via ex-situ scanning transmission electron microscopy (STEM) with respect to their morphology, particle size, and elemental distribution.

The sample derived from the precatalyst $LaNiO_3$ displays a distribution of spherical nickel particles on top of the lanthanum oxide support with a rounded morphology as shown by STEM measurements (Figure 9a, Figure 10a). The formation of such spherical particles by exsolution has been observed previously and was reported to occur predominantly at grain boundaries and stacking faults in the case of $LaNiO_3$.[45] In contrast, a coarser morphology with more edgy transition metal particles is present for the samples based on cobalt, which is most pronounced for the sample material derived from the precatalyst $La_{0.8}Sr_{0.2}CoO_3$ (Figure 9b–e). Surface analysis by X-ray photoelectron spectroscopy before and after catalysis shows that the ratio of La to Ni or Co does not change significantly, indicating that the reduced transition metals are not encapsulated in the La_2O_3 support (SI Figure S9). An inspection of the transition metal particle sizes shows that these are slightly smaller in the nickel-containing samples with an average particle diameter of 15 nm, while the cobalt particles have an average size of 42–46 nm (Table 2). The underlying distribution curves of the particle diameters can be found in the supporting information in Figure S10.

The average cobalt/nickel particle diameters obtained by ex-situ TEM are larger than the column length distributions determined for the crystallite sizes during the operando synchrotron experiments. The comparison of those values indicates, that the nickel particles are comprised of only a few crystallites, while the cobalt particles are composed out of many more crystallites.

Besides these spherical or rounded cobalt/nickel particles, regions with homogeneous cobalt/nickel dispersion on the support material are present in all samples (Figure 10). An exception is the sample material derived from the precatalyst $LaCo_{0.5}Ni_{0.5}O_3$, for which only a homogeneous distribution of cobalt and nickel on lanthanum oxide can be observed (Figure 10c). Pinzon et al. (2022) has also examined the particle size distribution of perovskites that have been reduced with 50 % H_2 in Ar (100 $mLmin^{-1}$) at 550 °C in a fixed-bed reactor and analyzed the transition metal particle size via TEM images.[13b] Those perovskites had been synthesized via self-combustion using citric acid as fuel. In this study, much smaller average transition metal particle sizes have been determined. This general difference might be explained by the varying experiment conditions, for example, the heating rate and the gas atmosphere. For cobalt derived from $LaCoO_3$, the average particle size amounted to 7.7 nm. Similar to our study, a smaller value was determined for nickel particles derived from $LaNiO_3$ with 4.2 nm.[13b]

The distribution of strontium and calcium does not seem to be linked to the distribution of metallic cobalt (Figure 10d–f). For a final understanding of the influence of strontium and calcium on the catalytic performance, their behavior during catalysis would need further investigation. Highly advanced

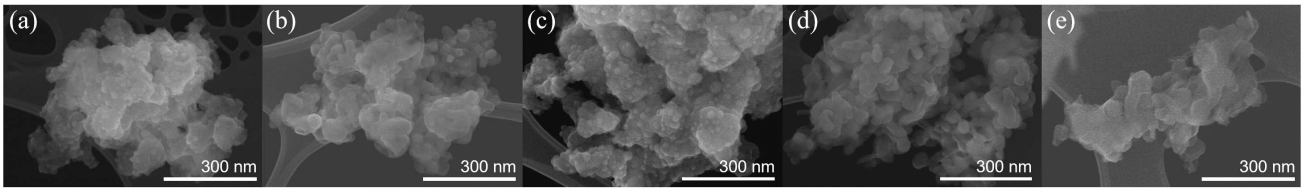

Figure 9. STEM images of samples after catalytic testing in the plug-flow reactor; the precatalyst compositions are (a) $LaNiO_3$, (b) $LaCoO_3$, (c) $LaCo_{0.5}Ni_{0.5}O_3$, (d) $La_{0.8}Ca_{0.2}CoO_3$, and (e) $La_{0.8}Sr_{0.2}CoO_3$.

Table 2. Size of the cobalt and nickel particles in the samples after the catalytic testing in the plug-flow-reactor derived by electron microscopy (STEM).

Sample derived from precatalyst:	Particle size* range of Co/Ni/nm	Average particle size* of Co/Ni/nm
$LaNiO_3$	10–32	15
$LaCoO_3$	20–90	42
$La_{0.8}Ca_{0.2}CoO_3$	20–160	46
$La_{0.8}Sr_{0.2}CoO_3$	25–60	43

* Particle size in this context means agglomerates or grains consisting of multiple crystallites.

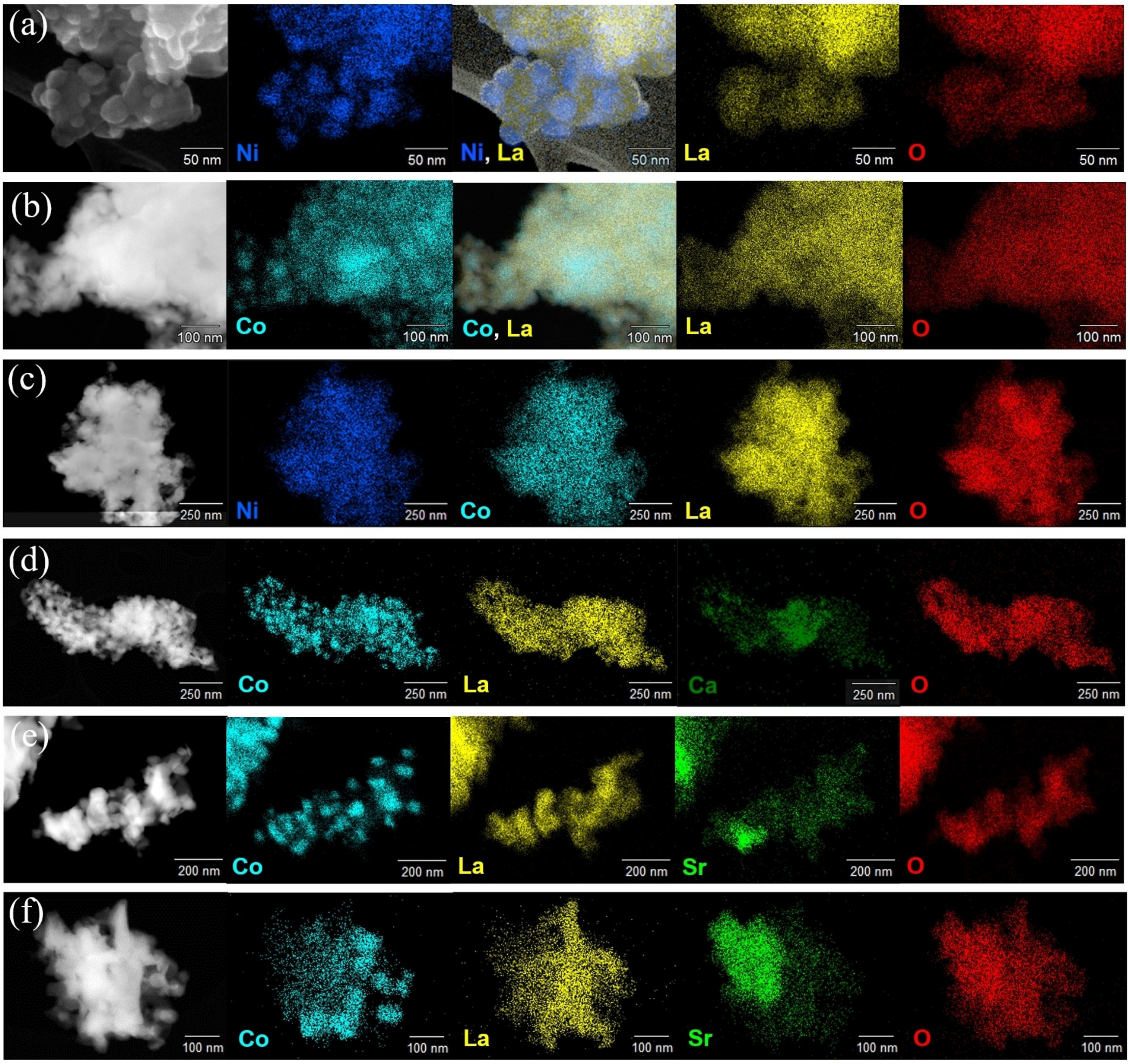

Figure 10. STEM-EDX images of the samples after catalytic testing in the plug-flow reactor; the precatalyst compositions are (a) $LaNiO_3$, (b) $LaCoO_3$, (c) $LaCo_{0.5}Ni_{0.5}O_3$, (d) $La_{0.8}Ca_{0.2}CoO_3$, and (e)–(f) $La_{0.8}Sr_{0.2}CoO_3$.

methods like *in situ* identical location TEM and further *operando* studies might give further insight.

Conclusions

This study shows the entire reaction pathway of perovskite precatalysts ABO_3 (A=La, Ca, Sr, and B=Fe, Co, Ni) via activation to the final catalyst. The results are based on *operando* synchrotron X-ray powder diffraction experiments performed under catalytic reaction conditions. The observed intermediate phases between the perovskites and the final reduction products Co^0/Ni^0 and La_2O_3 (CaO, SrO) are oxygen-depleted perovskite $A_3B_3O_8$, the brownmillerite phase $A_2B_2O_5$ and Ruddlesden-Popper phases $A_{n+1}B_nO_{3n+1}$. The higher the reducibility of the transition metal in the perovskite structure, the less distinct the intermediate phases form. In the case of the nickel-based perovskite activation, only the simultaneous formation and decomposition of a mixture of brownmillerite and Ruddlesden-popper phases could be approximated due to its highly dynamic character and the sample's easy reducibility. In contrast, when using the precatalyst $LaCoO_3$, both phases, $A_3B_3O_8$ and $A_2B_2O_5$, can be clearly identified. The partial substitution of lanthanum with strontium increased the reducibility of the cobalt-based perovskite so that only the brownmillerite was observable as an intermediate phase. The observed reaction behavior and the reaction pathway agree with the characteristics observed via TPR experiments.

Considering the catalytic performance, the composition $La_{0.8}Sr_{0.2}CoO_3$ resulted in the catalyst with the highest measured conversion for ammonia cracking. Therefore, substitutions of such type are a promising topic for future research. In detail, the calculated apparent activation energy of this sample is slightly higher with 100 $kJmol^{-1}$ compared to the lowest value of 90 $kJmol^{-1}$ for the one based on $LaNiO_3$. However, this circumstance is compensated by a large pre-exponential factor, which is determined to be 2.5 to 5 times higher for the sample containing strontium than for the other compositions. A possible explanation for this high conversion might be the crystallite sizes of La_2O_3 and Co^0, described in the form of column length distributions. A significant difference among all derived column length distributions is the shift to higher values for La_2O_3 in the sample with strontium substitution. This results in an increased crystallite size difference between La_2O_3 and the metallic cobalt, which might adjust the catalyst-support interaction positively. Moreover, strontium is known to affect the electronic properties of such catalysts advantageously. As strontium showed a much more positive effect on the catalytic performance than the lighter earth alkali metal calcium, a study testing the even heavier barium earth alkali metal as a promoter for perovskite precatalysts in ammonia decomposition might be worthwhile.

Experimental Section

Synthesis

Perovskites of the compositions $LaFeO_3$, $LaCoO_3$, $LaNiO_3$, $LaFe_{0.5}Ni_{0.5}O_3$, $LaFe_{0.5}Co_{0.5}O_3$, $LaCo_{0.5}Ni_{0.5}O_3$, $La_{0.8}Sr_{0.2}CoO_3$, and $La_{0.8}Ca_{0.2}CoO_3$, were synthesized by incipient wetness impregnation of commercial porous carbon spheres with nitrate solutions, subsequent drying, and calcination. This matrix-assisted preparation route in activated carbon was first reported by Schwickardi.[46] Mann+Hummel produced the carbon spheres, which Rütgers/CarboTech GmbH further treated for activation to make them hydrophilic. After activation, a specific surface area of 1800 $m^3 g^{-1}$ was determined by the Brunauer-Emmet-Teller (N_2-BET) method. Aqueous nitrate solutions were prepared by mixing deionized water with nitrate salts to get the following concentrations: 2.65 $molL^{-1}$ with $La(NO_3)_3$ * 6 H_2O (99,9% Alfa Aesar), 2.0 $molL^{-1}$ with $Ni(NO_3)_2$ * 6 H_2O (98% Alfa Aesar), 2.2 $molL^{-1}$ with $Co(NO_3)_2$ * 6 H_2O (>=98% Sigma Aldrich), 2.0 $molL^{-1}$ with $Sr(NO_3)_2$ (99.0% min. Alfa Aesar), 2.33 $molL^{-1}$ with $Fe(NO_3)_3$ * 9 H_2O (98+ % Alfa Aesar), and 2.7 $molL^{-1}$ with $Ca(NO_3)_2$ * 4 H_2O (99% Alfa Aesar). The solutions were mixed for each synthesis batch depending on the desired perovskite composition. The carbon spheres were stirred on a magnet plate while adding the premixed nitrate solution drop by drop until 80% of the pore volume was filled and then homogenized in an ultrasound bath for 30 min. After overnight drying at 50 °C, the impregnated carbon spheres were calcinated in a furnace. The first temperature step of 350 °C was reached with a heating rate of 2 $°Cmin^{-1}$ and held for 2 h. The heating was continued at a rate of 0.5 $°Cmin^{-1}$ up to 700 °C, held for 1 h, and then turned off. Because of problems upscaling the synthesis, smaller batches were prepared for each composition and mixed after quasi-identical quality was proven by X-ray powder diffraction.

X-ray Powder Diffraction

Ex-situ X-ray powder diffraction experiments were performed on a Malvern Pananalytical X'pert Pro diffractometer in Bragg-Brentano geometry with CuK_α radiation ($\lambda = 1.5406$ Å). The CuK_β radiation was eliminated with a Ni-filter. The anti-scatter slit was opened to 1/4 °, and the divergence slit to 1/8 °. The Soller slits were set to 0.04 rad, and a mask of 5 mm was used. A 15 mm steel sample holder was used for all measurements. The data were collected with a real-time multi-strip position-sensitive detector (X'Celerator) and a step width of 0.0167 ° 2θ per step. To measure Co- and Fe-containing samples, the detector's pulse height discrimination (PHD) level was changed from 36–80% to 49–80% to reduce the fluorescence contribution.

The *operando* synchrotron powder diffraction experiments under reaction conditions with NH_3 gas flow and simultaneous gas analysis were performed at beamline P02.1 at DESY. Data were collected with the Varex XRD 4343CT detector (150×150 μm^2 pixel size, 2880×2880 pixel area, CsI scintillator directly deposited on amorphous Si photodiodes) with an X-ray wavelength of $\lambda =$ 0.20735 Å, equivalent to 60 keV. The sample detector distance (SDD) was set to 120 cm. The sample environment consists of a gas flow cell built in-house that uses open-end quartz glass capillaries of 0.8 mm inner diameter and a wall thickness of 0.1 mm. The capillaries were filled with pellets made from our sample powders of 250–300 μm size with quartz glass wool before and after the sample to prevent it from being moved by the applied constant gas flow. The pellets were made by pressing the perovskite sample powder in a tablet of 1 cm diameter, breaking it apart, and retrieving the desired size fraction with a sieve tower. An exception was the measurement of the sample $LaFeO_3$, which was put as a powder into the capillary due to an insufficient sample amount for pressing a tablet and preparing pellets. Generally, a pellet shape has a lower risk of creating blockages of the gas flow in the capillary. In case they do occur, a pressure sensor was installed between the mass flow controller (MFC) and the capillary to detect them early and replace the sample capillary with a newly prepared one. An Oxford hot air blower, provided by the beamline, was installed 2 mm below the capillary. The gas flow was set to 5 $mLmin^{-1}$ of 100% NH_3 with a computer-controlled MFC by Bronkhorst, specifically suitable for the corrosive NH_3 gas. Two heating cycles were performed, of which the first one, also called the activation cycle, went from room temperature (RT) up to 650 °C with a constant heating rate of 10 $°Cmin^{-1}$. After cooling back to 350 °C, the second heating cycle was started, which consisted of 50 °C steps from 350 °C to 650 °C. Each step was measured for 15 min, and in between steps, the heating rate was again 10 $°Cmin^{-1}$. The data collection was done with 10 sec per frame. During both cycles, the outflowing gas was measured with a mass spectrometer (MS, Thermostar GSD 300T produced by Balzers) and a gas chromatograph (Micro GC Fusion produced by Inficon) for simultaneous gas analysis to determine the conversion rate for NH_3 decomposition qualitatively. The Micro GC Fusion has two channels, of which the first measures H_2, N_2, and O_2 using the carrier gas Ar. The second channel uses H_2 as the carrier gas, while NH_3 is measured. Both channels work with a thermal conductivity detector (TCD). The calculation of the NH_3 conversion based on the GC data is conducted by inserting the measured NH_3 volume-based percentage in a formula explained in the experimental section describing the catalytic experiments. The same formula is used to estimate the NH_3 conversion based on the MS data. In this case, the starting signal belonging to the mass-to-charge ratio of 15.9, which belongs to the NH^{2+} ion, is equated to 100% NH_3. At each temperature step, the remaining percentage of this value is calculated and again inserted in the abovementioned formula.

Reference crystal structures were taken from the Inorganic Crystal Structure Database provided by the FIZ Karlsruhe. The deposition numbers of the following structures are given in the references: $LaFeO_3$ (**1**), $LaCoO_3$ (**2**), $LaFe_{0.5}Co_{0.5}O_3$ (**3**), $LaNiO_3$ (**4**), $LaFe_{0.5}Ni_{0.5}O_3$ (**5**, **6**), $LaCo_{0.5}Ni_{0.5}O_3$ (**7**), $La_{0.8}Sr_{0.2}CoO_3$ (**8**), $La_{0.8}Ca_{0.2}CoO_3$ (**9**), Fe_2O_3 (**10**), Fe_3O_4 (**11**), Co_3O_4 (**12**), NiO (**13**). The structures of intermediate phases and final products of the perovskites' decompositions are $La_3Co_3O_8$ (**14**), $La_2Co_2O_5$ (**15**), CoO (**16**), Co (**17**), $La_4Ni_3O_{9.97}$ (**18**), $LaNiO_{2.5}$ (**19**), $La_4Ni_3O_{10}$ (**20**), $La_3Ni_2O_7$ (**21**), Ni (**22**), La_2O_3-cubic (**23**), La_2O_3-trigonal (**24**), SrO (**25**), CaO (**26**), and Fe_3N (**27**).[47]

Refinements, according to the Rietveld method, as well as the Whole Powder Pattern Modelling (WPPM) with Line Profile Analysis, were performed with the software TOPAS in the programming launch mode.[44,48] The data collected with a 2D detector at the synchrotron were integrated with the software DAWN.[49]

Temperature-Programmed Reduction

Temperature-programmed reduction experiments were performed with a Micromeritics AutoChem II 2920 instrument. It contains a thermal conductivity detector (TCD) to monitor changes in the thermal conductivity of the outflowing reducing gas mixture and, thus, changes in its composition after passing the sample. This way, reduction reactions taking place in the sample can be observed. Approximately 80 mg of each perovskite sample were prepared by heating up to 150 °C with 10 °Cmin^{-1} under Argon and holding at that temperature for 60 min. After cooling it to 50 °C again, the data were collected with a sampling interval of 1 sec while heating up to 800 °C with 10 °Cmin^{-1} under a gas flow of 50 cm^{3}min^{-1} with 10 % H_2 in Argon.

Catalytic Experiments

Catalytic conversion measurements for NH_3 cracking were performed in a 6 mm inner diameter plug-flow reactor with an attached 3000 Micro GC by Agilent Technologies for gas analysis. A schematic view of the setup can be found in the supporting information (SI Figure S11). Like the Micro GC Fusion by Inficon used during the *operando* synchrotron powder diffraction experiments under reaction conditions, it has two columns with the carrier gases Ar and H_2 to measure H_2, N_2, O_2, and NH_3. It uses TCDs as well. For approximately 50 mg of perovskite sample powder, a 100 % NH_3 gas flow with a weight hour space velocity of 15000 mLg^{-1}h^{-1} was applied. The temperature program consists of 3 cycles with a heating rate of 20 °Cmin^{-1}. The first cycle consists of heating from RT to 350 °C and up to 650 °C in 50 °C steps. Each step is held for 40 min for equilibration purposes and due to the relatively long time of 3 min per measurement of the GC. The NH_3 cracking conversion is calculated by inserting the normalized NH_3 volume-based percentage x/Vol-% of the outflowing gas into the following formula, which is derived from the stoichiometry of the decomposition reaction ($2\,NH_3 \rightarrow 3\,H_2 + N_2$):

$$Conversion/\% = \frac{1-\frac{2x}{100}^{*}}{1+\frac{x}{100}}\ 100$$

The calculated conversion values of each temperature step's last five GC measurements are averaged. After cooling to 350 °C, a second cycle of heating in 50 °C steps up to 650 °C is measured. A third cycle is repeated in the same manner. Two batches of these experiments are conducted for the perovskite samples. During the first one, a space velocity calculated based on the weight of the whole perovskite is applied. In the second batch, the perovskites that decompose to a metallic transition metal as the active catalytic phase and La_2O_3 were measured again but with the space velocity based only on the weight of the transition metal within the perovskite. These three cycles were followed up by a conversion stability test consisting of holding 550 °C for 20 h. These measurements were also used to calculate the apparent activation energy E_a [kJmol^{-1}] and the pre-exponential factor A [s^{-1}].

Electron Microscopy

The scanning electron microscopy (STEM) measurements with optional energy dispersive X-ray (EDX) spectroscopy for (quantitative) elemental analysis were conducted on a Hitachi S-5500 instrument running on 30 kV with an UltraDry detector. The pick-up angle was 15.1 degrees, and a Cliff-Lorimer (MBTS) based correction method without considering the absorption was applied.

Acknowledgements

We thank the Max Planck Society for basic funding. We also acknowledge DESY (Hamburg, Germany), a member of the Helmholtz Association HGF, for the provision of experimental facilities. Parts of this research were carried out at PETRA III, and we would like to thank Ph.D. Alba San Jose Mendez for assistance in using beamline P02.1. Beamtime was allocated for proposal I-20211254. We want to thank Dr. Wolfgang Schmidt, Jan Ternieden, Tobias Rathmann, and Isabella Kappel for their help in performing the synchrotron experiments. S.G. is also grateful to Dr. Hilke Petersen for the scientific discussion and for supporting Rietveld refinements. We also thank Alexander Kostis for providing the electron microscopy measurements. Open Access funding enabled and organized by Projekt DEAL.

Conflict of Interests

The authors declare no conflict of interest.

Data Availability Statement

The data that support the findings of this study are available from the corresponding author upon reasonable request.

Keywords: Ammonia · Perovskite phases · Supported catalysts · In situ X-ray diffraction · Exsolution

[1] J. O. Abe, A. P. I. Popoola, E. Ajenifuja, O. M. Popoola, *Int. J. Hydrogen Energy* **2019**, *44*, 15072–15086.

[2] A. Zuttel, A. Remhof, A. Borgschulte, O. Friedrichs, *Phil. Trans. R. Soc. A* **2010**, *368*, 3329–3342.

[3] Z. Abdin, C. G. Tang, Y. Liu, K. Catchpole, *iScience* **2021**, *24*, 23.

[4] S. Chatterjee, R. K. Parsapur, K. W. Huang, *ACS Energy Lett.* **2021**, *6*, 4390–4394.

[5] A. Klerke, C. H. Christensen, J. K. Norskov, T. Vegge, *J. Mater. Chem.* **2008**, *18*, 2304–2310.

[6] a) T. E. Bell, G. W. Zhan, K. J. Wu, H. Zeng, L. Torrente-Murciano, *Top. Catal.* **2017**, *60*, 1251–1259; b) W. U. Khan, H. S. Alasiri, S. A. Ali, M. M. Hossain, *Chem. Rec.* **2022**, *22*, 18; c) C. Q. Chen, K. Wu, H. J. Ren, C. Zhou, Y. Luo, L. Lin, C. T. Au, L. L. Jiang, *Energ. Fuel* **2021**, *35*, 11693–11706.

[7] a) Y. Q. Gu, Y. L. Ma, Z. Y. Long, S. Zhao, Y. Wang, W. C. Zhang, *Int. J. Hydrogen Energy* **2021**, *46*, 4045–4054; b) G. R. Li, X. T. Yu, Z. P. Lei, F. X. Yin, H. F. Zhang, X. B. He, *Catal. Lett.* **2022**, 1–11; c) K. Okura, K. Miyazaki,

H. Muroyama, T. Matsui, K. Eguchi, *RSC Adv.* **2018**, *8*, 32102–32110; d) Y. Qiu, E. K. Fu, F. Gong, R. Xiao, *Int. J. Hydrogen Energy* **2022**, *47*, 5044–5052; e) ; H. Tabassum, S. Mukherjee, J. J. Chen, D. Holiharimanana, S. Karakalos, X. X. Yang, S. Hwang, T. Y. Zhang, B. Lu, M. Chen, Z. Tang, E. A. Kyriakidou, Q. F. Ge, G. Wu, *Energ. Environ. Sci.***2022**, *15*, 4190–4200; f) C. Weidenthaler, W. Schmidt, S. Leiting, J. Ternieden, A. Kostis, T. H. Ulucan, E. Budiyanto, *ChemCatChem* **2022**, *14*, 9.

[8] M. Pinzon, A. Sanchez-Sanchez, P. Sanchez, A. R. de la Osa, A. Romero, *Energ. Convers. Manage.* **2021**, *246*, 12.

[9] a) J. W. Zhang, M. R. Gao, J. L. Luo, *Chem. Mater.* **2020**, *32*, 5424–5441; b) J. H. Kim, J. K. Kim, J. Liu, A. Curcio, J. S. Jang, I. D. Kim, F. Ciucci, W. Jung, *ACS Nano* **2021**, *15*, 81–110; c) B. Rudolph, A. I. Tsiotsias, B. Ehrhardt, P. Dolcet, S. Gross, S. Haas, N. D. Charisou, M. A. Goula, S. Mascotto, *Adv. Sci.* **2023**, *10*.

[10] D. Neagu, T. S. Oh, D. N. Miller, H. Menard, S. M. Bukhari, S. R. Gamble, R. J. Gorte, J. M. Vohs, J. T. S. Irvine, *Nat. Commun.* **2015**, *6*.

[11] T. Ruh, D. Berkovec, F. Schrenk, C. Rameshan, *Chem. Commun.* **2023**, *59*, 3948–3956.

[12] a) Y. Y. Li, Y. S. Zhang, K. Qian, W. X. Huang, *ACS Catal.* **2022**, *12*, 1268–1287; b) N. Jeon, S. Kim, A. Tayal, J. Oh, W. Yoon, W. B. Kim, Y. Yun, *ACS Sustainable Chem. Eng.* **2022**, *10*, 15564–15573; c) C. F. Cao, K. Wu, C. Zhou, Y. H. Yao, Y. Luo, C. Q. Chen, L. Lin, L. L. Jiang, *Chem. Eng. Sci.* **2022**, *257*, 8.

[13] a) S. Podila, H. Driss, A. M. Ali, A. A. Al-Zahrani, M. A. Daous, *Arab. J. Chem.* **2022**, *15*, 10; b) M. Pinzon, A. Sanchez-Sanchez, A. Romero, A. R. de la Osa, P. Sanchez, *Fuel* **2022**, *323*, 13.

[14] J. C. Ganley, F. S. Thomas, E. G. Seebauer, R. I. Masel, *Catal. Lett.* **2004**, *96*, 117–122.

[15] O. A. Al-attar, S. Podila, A. A. Al-Zahrani, *Arabian J. Sci. Eng.* **2022**, 1–11.

[16] V. M. Goldschmidt, *Naturwissenschaften* **1926**, *14*, 477–485.

[17] a) B. Echchahed, S. Kaliaguine, H. S. Alamdari, *Int. J. Chem. React. Eng.* **2006**, *4*; b) S. Ivanova, A. Senyshyn, E. Zhecheva, K. Tenchev, R. Stoyanova, H. Fuess, *J. Solid State Chem.* **2010**, *183*, 940–950; c) M. M. Nair, S. Kaliaguine, F. Kleitz, *ACS Catal.* **2014**, *4*, 3837–3846.

[18] J. Suntivich, W. T. Hong, Y. L. Lee, J. M. Rondinelli, W. L. Yang, J. B. Goodenough, B. Dabrowski, J. W. Freeland, Y. Shao-Horn, *J. Phys. Chem. C* **2014**, *118*, 1856–1863.

[19] J. G. He, C. Franchini, *Phys. Rev. B* **2012**, *86*.

[20] a) O. H. Hansteen, H. Fjellvag, B. C. Hauback, *J. Mater. Chem.* **1998**, *8*, 2081–2088; b) M. Kuras, R. Roucou, C. Petit, *J. Mol. Catal. A* **2007**, *265*, 209–217.

[21] C. L. Guo, J. L. Zhang, X. L. Zhang, *React. Kinet. Catal. Lett.* **2008**, *95*, 89–97.

[22] D. C. D. Lima, I. P. Lemos, R. S. Gomes, L. Rodrigues, R. T. Frety, C. Resini, B. S. Roberto, S. T. Brandao, *Catal. Lett.* **2022**, 1–12.

[23] M. Crespin, W. K. Hall, *J. Catal.* **1981**, *69*, 359–370.

[24] R. Spinicci, A. Tofanari, A. Delmastro, D. Mazza, S. Ronchetti, *Mater. Chem. Phys.* **2002**, *76*, 20–25.

[25] H. Provendier, C. Petit, C. Estournes, S. Libs, A. Kiennemann, *Appl. Catal. A* **1999**, *180*, 163–173.

[26] T. Arima, Y. Tokura, J. B. Torrance, *Phys. Rev. B* **1993**, *48*, 17006–17009.

[27] P. Ciambelli, S. Cimino, S. De Rossi, L. Lisi, G. Minelli, P. Porta, G. Russo, *Appl. Catal. B* **2001**, *29*, 239–250.

[28] G. Munteanu, L. Ilieva, D. Andreeva, *Thermochim. Acta* **1997**, *291*, 171–177.

[29] S. M. de Lima, J. M. Assaf, *Catal. Lett.* **2006**, *108*, 63–70.

[30] a) R. Caciuffo, D. Rinaldi, G. Barucca, J. Mira, J. Rivas, M. A. Senaris-Rodriguez, P. G. Radaelli, D. Fiorani, J. B. Goodenough, *Phys. Rev. B* **1999**, *59*, 1068–1078; b) M. Liu, X. L. Yang, Z. M. Tian, H. M. Wang, L. T. Yin, J. J. Chen, Q. Q. Guan, H. Yang, Q. L. Zhang, *Phys. Chem. Chem. Phys.* **2022**, *24*, 3686–3694.

[31] L. Guo, L. Bo, Y. Li, Z. Jiang, Y. Tian, X. Li, *Solid State Sci.* **2021**, *113*.

[32] M. Rojas, G. Bernales, A. B. Dongil, G. Pecchi, N. Escalona, *New J. Chem.* **2022**, *46*, 21181–21189.

[33] S. Irusta, M. P. Pina, M. Menendez, J. Santamaria, *J. Catal.* **1998**, *179*, 400–412.

[34] J. C. Grenier, J. Darriet, M. Pouchard, P. Hagenmuller, *Mater. Res. Bull.* **1976**, *11*, 1219–1226.

[35] K. Vidyasagar, A. Reller, J. Gopalakrishnan, C. N. R. Rao, *J. Chem. Soc. Chem. Commun.* **1985**, 7–8.

[36] a) M. Fang, S. P. Kelty, X. M. He, *Ionics* **2014**, *20*, 1111–1116; b) A. F. Andreeva, I. Gil'Man, *Inorg. Mater.* **1978**, *14*, 384–390; c) P. Aldebert, J. P. Traverse, *Mater. Res. Bull.* **1979**, *14*, 303–323.

[37] J. Felsche, *Naturwissenschaften* **1969**, *56*, 212-&.

[38] V. B. Glushkova, E. K. Keler, *Dokl. Akad. Nauk SSSR* **1963**, *152*, 611-&.

[39] G. Brauer, E. Mohr-Rosenbaum, *Z. Anorg. Allg. Chem.* **1972**, *394*, 301–304.

[40] N. Imanaka, T. Masui, Y. Kato, *J. Solid State Chem.* **2005**, *178*, 395–398.

[41] J. L. Hueso, J. P. Holgado, R. Pereniguez, V. M. Gonzalez-DelaCruz, A. Caballero, *Mater. Chem. Phys.* **2015**, *151*, 29–33.

[42] P. Steiger, O. Krocher, D. Ferri, *Appl. Catal. A* **2020**, *590*.

[43] J.-C. Tseng, D. Gu, C. Pistidda, C. Horstmann, M. Dornheim, J. Ternieden, C. Weidenthaler, *ChemCatChem* **2018**, *10*, 4465–4472.

[44] P. Scardi, M. Leoni, *Acta Crystallogr. Sect. A* **2002**, *58*, 190–200.

[45] P. Cao, P. Tang, M. F. Bekheet, H. Du, L. Yang, L. Haug, A. Gili, B. Bischoff, A. Gurlo, M. Kunz, *J. Phys. Chem. C* **2021**, *126*, 786–796.

[46] M. Schwickardi, T. Johann, W. Schmidt, F. Schuth, *Chem. Mater.* **2002**, *14*, 3913–3919.

[47] a) G. Bergerhoff, I. D. Brown, F. Allen, *IUCR, Chester* **1987**, *360*, 77–95; b) Deposition numbers 1644911 (for **1**), 1698345 (for **2**), 2147596 (for **3**), 1653369 (for **4**), 1712697 (for **5**), 1712698 (for **6**), 1668001 (for **7**), 1642872 (for **8**), 1713844 (for **9**), 1688577 (for **10**), 1636271 (for **11**), 1600256 (for **12**), 825069 (for **13**), 1646078 (for **14**), 1616091 (for **15**), 1594774 (for **16**), 1749830 (for **17**), 1928599 (for **18**), 1643008 (for **19**), 1650706 (for **20**), 1650704 (for **21**), 1762099 (for **22**), 1759816 (for **23**), 1620979 (for **24**), 710595 (for **25**), 1719622 (for **26**), and 1680034 (for **27**) contain the supplementary crystallographic data for this paper. These data are provided free of charge by the joint Cambridge Crystallographic Data Centre and Fachinformationszentrum Karlsruhe Access Structures service.

[48] a) L. B. McCusker, R. B. Von Dreele, D. E. Cox, D. Louer, P. Scardi, *J. Appl. Crystallogr.* **1999**, *32*, 36–50; b) Bruker-AXS, **2017**; c) A. A. Coelho, *J. Appl. Crystallogr.* **2018**, *51*, 210–218.

[49] a) M. Basham, J. Filik, M. T. Wharmby, P. C. Chang, B. El Kassaby, M. Gerring, J. Aishima, K. Levik, B. C. Pulford, I. Sikharulidze, *J. Synchrotron Radiat.* **2015**, *22*, 853–858; b) J. Filik, A. Ashton, P. Chang, P. Chater, S. Day, M. Drakopoulos, M. Gerring, M. Hart, O. Magdysyuk, S. Michalik, *J. Appl. Crystallogr.* **2017**, *50*, 959–966.

Manuscript received: July 25, 2023
Revised manuscript received: September 14, 2023
Accepted manuscript online: September 22, 2023
Version of record online: October 2, 2023